

THE GINI COEFFICIENT AS A MORPHOLOGICAL MEASUREMENT OF STRONGLY LENSED GALAXIES IN THE IMAGE PLANE

MICHAEL K. FLORIAN^{1,2}, NAN LI^{1,2,3}, AND MICHAEL D. GLADDERS^{1,2}

Draft version May 22, 2022

ABSTRACT

Characterization of the morphology of strongly lensed galaxies is challenging because images of such galaxies are typically highly distorted. Lens modeling and source plane reconstruction is one approach that can provide reasonably undistorted images on which morphological measurements can be made, although at the expense of a highly spatially variable telescope PSF when mapped back to the source plane. Unfortunately, modeling the lensing mass is a time and resource intensive process, and in many cases there are too few constraints to precisely model the lensing mass. If, however, useful morphological measurements could be made in the image plane rather than the source plane, it would bypass this issue and obviate the need for a source reconstruction process. We examine the use of the Gini coefficient as one such measurement. Because it depends on the cumulative distribution of the light of a galaxy, but not the relative spatial positions, the fact that surface brightness is conserved by lensing means that the Gini coefficient may be well-preserved by strong gravitational lensing. Through simulations, we test the extent to which the Gini coefficient is conserved, including by effects due to PSF convolution and pixelization, to determine whether it is invariant enough under lensing to be used as a measurement of galaxy morphology that can be made in the image plane.

1. INTRODUCTION

Studying galaxies over the course of cosmic time requires making many measurements—broadband colors, spectra, emission and absorption lines and the implied chemical abundances, star formation rates, and stellar populations, and more. Among the observables of interest is, of course, morphology, which is of particular relevance because of its possible relationships with both galaxy and star formation (e.g., Dressler 1980; Abraham et al. 1996; Willett et al. 2015).

While morphologies of low redshift galaxies can be studied in great detail, high redshift galaxies present a challenge because of their small angular sizes. Even with the increased signal to noise ratios (S/N) and resolutions of the James Webb Space Telescope (JWST) and the Wide-Field Infrared Survey Telescope (WFIRST), this will continue to be a limitation at large redshifts. A desire to study small-scale structures in high redshift galaxies has led some to take advantage of the extra magnification provided by strong gravitational lensing (e.g., Wuyts et al. 2014; Swinbank et al. 2009; Jones et al. 2010, 2013).

Much effort has been put into quantifying the morphological properties of galaxies. Current morphological metrics include the CAS system which consists of the concentration parameter, the asymmetry parameter and the clumpiness parameter as described by Conselice (2003) and references therein, as well as the Gini coefficient (Abraham et al. 2003), and the internal color dispersion (Papovich et al. 2003). However, the definitions of many of these measurements depend on the relative amplitude *and* position of a galaxy’s light, and

so are unlikely to be useful when applied directly to strongly lensed images of distant galaxies. Given a lens model, such images can be mapped back to the undistorted source plane, but creating models that allow for the reconstruction of the source galaxy can be a difficult and time consuming process and even when mass models can be constructed with low levels of uncertainty, uncertainties in magnification maps can still be much higher. Moreover, simple source plane reconstruction techniques, absent some form of point spread function (PSF) deconvolution, will also map a telescope PSF that is reasonably invariant in the image plane into a highly distorted and variable PSF in the source plane, potentially complicating any morphological analysis. And, while many techniques exist for modeling lenses (see Lefor et al. 2013 for a review), in some cases there are simply not enough constraints to make a lens model possible at all without major uncertainties. When sufficient constraints are available, it can still take many hours of focused effort for a researcher or group to produce a final model. This modeling, required before reconstruction of the undistorted source galaxy can be attempted, represents a major bottleneck in the process of making morphological measurements of strongly lensed galaxies. This difficulty will only become more severe as the next generation of ground- and space-based survey telescopes comes online and brings our samples of strong lensing systems into the thousands.

To avoid this difficulty altogether, it is worth seeking out morphological measurements that can be performed in the image (lensed) plane rather than the source (unlensed) plane. In this paper, we show through simulation that the Gini coefficient, introduced to astronomy and used for classifying galaxy morphologies in the Sloan Digital Sky Survey (SDSS) by Abraham et al. (2003), is one such measurement. Furthermore, we show that a relationship exists between lensed and unlensed Gini coefficients for a given source image with a resolution

¹ Department of Astronomy and Astrophysics, University of Chicago, Chicago, IL 60637

² Kavli Institute for Cosmological Physics, The University of Chicago, Chicago, IL 60637

³ Argonne National Laboratory, 9700 South Cass Avenue B109, Lemont, IL 60439

similar to images taken by the Hubble Space Telescope (HST) as long as the apertures are carefully defined using a prescription like the one given in section 2.3 of this paper. This relationship allows us to finally investigate the question of how the currently known lensed galaxies compare, morphologically, with their unlensed counterparts at similar redshifts, which will be the focus of a future paper.

2. TESTING THE STABILITY OF THE GINI COEFFICIENT: THE SIMULATIONS

The Gini coefficient, as applied to galaxy morphologies, is a measurement of the inequality of the distribution of light in a galaxy. Conceptually, this measurement is made by ordering the pixels that make up the image of a galaxy in ascending order by flux and then comparing the resulting cumulative distribution function to what would be expected from a perfectly even flux distribution. A low Gini coefficient (close to zero) means that the distribution of light is fairly uniform, while a high Gini coefficient (close to one) means that most of the galaxy's light is contained in only a small fraction of the pixels. In practice, the Gini coefficient is calculated using the following formula from Abraham et al. (2003):

$$G = \frac{1}{\bar{X}n(n-1)} \sum_{i=1}^n (2i - n - 1)X_i \quad (1)$$

where X_i is the value of the i^{th} pixel when ordered by flux, \bar{X} is the mean of the pixel values, and n is the total number of pixels. Because gravitational lensing preserves surface brightness, the cumulative distribution of the light should be little changed, and the Gini coefficient can be expected to be fairly well preserved by lensing.

This hypothesis was tested by simulating the lensing effect on actual images of low redshift galaxies treated as if they were galaxies at higher redshifts using steps which will be explained in further detail in the following sections. Briefly stated, a set of 33 detailed images of low redshift galaxies ($z \lesssim 0.45$) were chosen from the CANDELS UDS field (Galametz 2013). Those galaxies were placed at higher redshifts and on or near caustics of a galaxy cluster scale lensing mass and run through a gravitational lensing simulation code to produce arcs of a similar size to those seen in observations. These final images of the arcs were then convolved with an HST-like PSF and rebinned to a pixel scale of 0.03 arcseconds/pixel. Varying amounts of noise were added to the images, and masks were made based on a generalization of the Petrosian radius defined in such a way as to be applicable to objects of arbitrary shape. Within these apertures, Gini coefficients were calculated and compared in a variety of ways which will be detailed in section 3.

2.1. Galaxy Selection

The 33 galaxies that were used as sources in the lensing simulation were selected from the CANDELS UDS field (Galametz 2013). They were chosen to span a range of morphologies (11 ellipticals, 20 spirals, and 2 irregular galaxies). We chose galaxies that are low redshift, and large on the sky, so that detailed images of small scale structures were available. Before lensing, an aperture was made based on a 12σ threshold on the stack of the F160W, F814W and F606W images, which, given

the high signal-to-noise ratios in the CANDELS UDS images, still included most of the light associated with each galaxy. Pixels outside of these apertures were set to zero, minimizing the number of pixels that needed to be treated by the gravitational lensing ray-tracing code while also isolating the target galaxies from nearby objects.

2.2. Simulating Gravitational Lensing by Ray-Tracing

In our gravitational lensing image simulation, the lensing mass had a spherical NFW profile with virial mass $M_{200} = 10^{15} M_{\odot}/h$ and concentration parameter $c = 5$. The lensing mass was placed at redshift $z_l = 0.2$. The source plane was located at $z_s = 1.0$. Because they were actually observed at a redshift much closer to 0, the 33 galaxies selected from the CANDELS UDS field were treated as though each pixel was 0.0075 arcseconds in the source plane even though the original images were drizzled to a 0.03 arcsecond/pixel resolution. For each galaxy we picked 50 random positions inside an 8 arcsecond square grid, centered on the lens so that the image positions would be close to caustics. For images of each galaxy in each of 3 filters (F160W, F814W, and F606W), the ray-tracing was performed using the code described by Li et al. (2015) at each of the 50 source positions, resulting in 4950 total lensed images (33 galaxies \times 50 positions \times 3 filters). At this stage, the images were sampled to a 0.01 arcsecond pixel grid.

The images produced by the ray-tracing code have a much finer pixel scale than could actually be observed with the Hubble Space Telescope. To create images similar to what would actually be observed, these images were convolved with a Gaussian PSF with the same FWHM as the HST PSF and rebinned to a final scale of 0.03 arcseconds per pixel. To test the effects of performing observations with different S/N per pixel, noise was added to each of the resultant arc images. For each arc, an image was produced with S/N per pixel of $10^{-3.5}$ through 10^1 in steps of $10^{0.5}$, yielding 10 images with different average S/N per pixel for each arc. These logarithmic bins were chosen to correspond encompass the range of S/N levels typical of observations performed with HST. Thus, in summary, our database of simulated strongly lensed images includes nearly 50,000 individual frames (33 galaxies \times 50 positions \times 3 filters \times 10 S/N levels) and many more individual arcs due to the high occurrence of systems with multiple images.

2.3. Generalizing the Petrosian Radius to Isolate Arcs

Lisker (2008) found that the size of the aperture inside which the Gini coefficient is calculated can have a significant effect on the measured value of the Gini coefficient. Use too small of an aperture and only part of the galaxy is used for the measurement. Use too large of an aperture and so much sky is included that the Gini coefficient will be biased toward values near 1. Lisker (2008) measured Gini coefficients using elliptical Petrosian apertures of various sizes (i.e., using apertures defined using multiples of the Petrosian semimajor axis, which is used in place of a Petrosian radius). Apertures that best balanced inclusion of galactic light with exclusion of sky and therefore maximized the differences between Gini coefficients of different objects were found to be constructed

from semimajor axes that fell between 2/3 and 1 times the Petrosian semimajor axis.

In light of these results, it is important to define a similarly inclusive aperture for arcs that also avoid including too many sky pixels. To do this, the definition of the Petrosian radius used by the Sloan Digital Sky Survey (Blanton et al. 2001; Yasuda et al. 2001) was adopted and then reformulated in terms of areas (rather than radii) in order to find apertures for galaxies whose shapes were severely distorted by strong gravitational lensing.

The Petrosian radius as used by SDSS is defined implicitly by the following equation from Yasuda et al. (2001):

$$\eta = \frac{2\pi \int_{0.8r_p}^{1.25r_p} I(r)rdr / \{\pi[(1.25r_p)^2 - (0.8r_p)^2]\}}{2\pi \int_0^{r_p} I(r)rdr / (\pi r_p^2)} \quad (2)$$

where $\eta = 0.2$, $I(r)$ is the surface brightness profile of the galaxy, r is the radius over which we are integrating, and r_p is the Petrosian radius. Essentially, this compares the average surface brightness within an annulus with an inner radius of $0.8r$ and outer radius of $1.25r$ to the average surface brightness in the circle of radius r . When the ratio of these two values (the Petrosian ratio) is 0.2, r is the Petrosian radius.

This understanding of the Petrosian ratio leads very naturally to a redefinition in terms of areas. We look for an annulus with an area equal to $[2\pi(1.25r)^2 - 2\pi(0.8r)^2]/[2\pi r^2]$ or simply $(1.25^2 - 0.8^2)$ times the area of the circle of radius r . The average surface brightness within the annulus is then compared to the average surface brightness within the full circle. When the ratio is 0.2, r is the Petrosian radius. With this reformulation in terms of areas, we extend the definition of a Petrosian aperture to include any arbitrary (connected) shape. To do this, we take a shape, calculate its area in pixels, and build contours either inward or outward until the area of the contours contains $(1.25^2 - 0.8^2)$ times the number of pixels that the original shape did. When the ratio of the average surface brightness of the outer contour is 0.2 times that of the inner shape, we have found an aperture analogous to the one defined by the Petrosian radius. Defining the initial shape of the aperture, from which we build inward or outward (usually outward), requires nothing more than thresholding. For these simulations, we used a threshold of 2.5σ above the background. Fig. 1 shows the aperture produced by this method for an unlensed elliptical galaxy, compared to the elliptical Petrosian aperture produced for the same galaxy by Source Extractor. Each simulated lensed image was masked using this method. In some cases, especially those for which the S/N per pixel was very low, defining apertures in this manner was not possible. At extremely low S/N, the initial aperture shape determined by thresholding does not necessarily follow the light distribution of the galaxy, since it is more easily influenced by the sky noise. As a result, these starting apertures can be quite large and quickly grow past the size of the simulated image before the Petrosian ratio falls to 0.2. Alternatively, the starting aperture could be too small (if, for example, part of the arc is very bright, but the rest is faint) and as a result, the shape of the aperture will not accurately reflect the shape of the arc and parts of the arc may not be included. Instances like this were

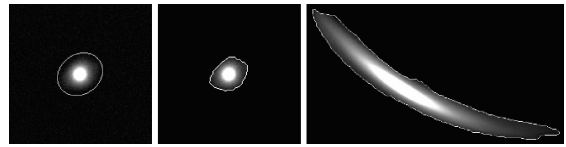


FIG. 1.— *Left:* An elliptical galaxy and its Petrosian ellipse as determined by Source Extractor. *Center:* The same galaxy with its aperture determined using the method from this paper. *Right:* The same galaxy after being lensed and masked using the method from this paper.

rare and typically occurred only at the lowest two S/N levels that we tested and for the vast majority of lensed images, there were no problems.

2.4. Measuring the Gini Coefficients

Finally, for each image of each galaxy in each filter and S/N per pixel bin, the Gini coefficient and its associated uncertainty was measured according to the prescription in Abraham et al. (2003) within apertures defined as in Section 2.3. For moderate to high S/N levels, changing the threshold of the cut used to determine the shape of the aperture from 2.5σ to 1.5σ or to 3.5σ resulted in changes to the measured Gini coefficient of only about 2–3%. As we will show in Section 3.1, such a change is still small compared to the slight variation in the measured Gini coefficient between different lensing model realizations of the same source galaxy and is therefore not a significant source of uncertainty. However, at the very lowest S/N levels, the aperture shape can vary greatly depending on the threshold chosen, but at such low S/N levels, the sky dominates the measurement of the Gini coefficient anyway and renders it useless regardless of aperture shape.

3. RESULTS

Before the analysis was carried out, two cuts were made on the simulated images in order to ensure that the sample was as close as possible to what would exist in an observed sample. First, any images that were magnified by less than a factor of 4 were removed. This mostly removed central, demagnified images that would not be observed in real data. It also removed images where a piece of sky noise in the original unlensed CANDELS image fell on a caustic and resulted in a large image of something that wasn't actually the galaxy. The second cut was to remove all central images and radial images so that the analysis could focus entirely on tangential arcs and counter images, which are far more likely to be observed without significant contamination from light from the intervening lens in practice. We plot, in Fig. 2, the distance (in arcseconds) of the point in each of the arcs in our sample that is closest to the center of the lensing halo. We find 4 regions. The innermost images are central images and have distances of nearly zero, which are often demagnified and unobservable. There is another bump in the histogram centered near $3''$, where the radial arcs lie. Then there are two more clearly defined peaks at around 6–18 and 20–30 arcseconds, corresponding to the counterimages and the tangential arcs, respectively. A cut was made in this space at $6.5''$, removing anything closer so that only tangential arcs and counterimages were included in the sample. All of the following results are drawn from the sample of strongly lensed galaxy images that remained after these two cuts.

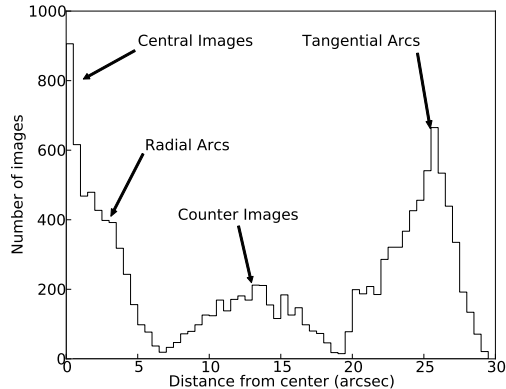


FIG. 2.— Distribution of the distances, in arcseconds, of the nearest point on each lensed image to the center of the lensing halo. We see four nearly distinct distributions consisting of central images, radial arcs, counter images, and tangential arcs, which allows tangential arcs and counter images to be identified using a cut based on this distance.

3.1. Relationship Between Unlensed Gini Coefficient and Lensed Gini Coefficient

We consider first the relationship between the Gini coefficient of the unlensed source galaxy and the Gini coefficient of the corresponding simulated lensed galaxy images. We used, for the unlensed Gini coefficient, the Gini coefficient of the source galaxy as if it were placed at the same redshift as the source galaxies used in the simulation. This required resampling the image to reduce the pixel scale by about a factor of 3 (reducing the total image size by a factor of 9). In other words we convolved the images with a Gaussian PSF with FWHM equal to the width of the PSF of HST WFC3 images taken in the corresponding filter (either F160W, F814W, or F606W), then rebinned the resulting images from a 0.01 arcseconds/pixel resolution to 0.03 arcseconds/pixel and added noise as we did with the lensed images (see Section 2.2). These unlensed images were then masked using the same method as was used for the lensed images.

For each source galaxy, in each S/N ratio bin and in each filter, the median Gini coefficient of all of the lensed images of that galaxy was plotted against its unlensed Gini coefficient. The resulting plot for model realizations in the 0.1 S/N per pixel bin is shown in Fig. 3. Uncertainties in the median lensed Gini coefficients are simply the standard deviation in the distribution of Gini coefficients for lensed images of that particular source galaxy in the relevant filter. The uncertainty in the unlensed Gini coefficient for each galaxy is calculated using the bootstrapping method described in Abraham et al. (2003). Best fit lines for each filter were calculated using a maximum likelihood technique with weighting for each point determined by uncertainties. While each filter has a slightly different slope and y-intercept, these parameters are relatively unchanged by the S/N per pixel values in the high S/N bins. This relationship is shown in Fig. 4 (note that a slight spacing in the S/N per pixel axis has been introduced for clarity). Uncertainties were again determined by bootstrapping the selection of source galaxies used in the trendline analysis. At most S/N levels higher than about 0.01/pixel, the best fitting parameters do not vary significantly with S/N.

Furthermore, the two UVIS filters (which had very similar PSFs and whose PSFs were sharper than for the IR filter) are indistinguishable from each other. The slope of the best fit line for the F160W filter images tends to be shallower than for the other two filters regardless of S/N level until the noise becomes very high. Therefore to characterize the relationship between the lensed and unlensed Gini coefficients, we fit one line to the UVIS (sharper PSF) data and another line to the IR (broader PSF) data. In each case, the lines were fit to a dataset consisting of all points from all 6 S/N levels greater than 0.01 using a maximum likelihood technique with the significance of each point weighted according to the uncertainties in the lensed and unlensed Gini coefficients. All points used in this analysis are shown in Fig. 5 along with the best fit lines for the IR sample, the UVIS sample, and the entire sample. The following are the equations describing the best fit lines where UGC is the unlensed Gini coefficient and LGC is the lensed Gini coefficient:

$$\begin{aligned} \text{IR: } \text{UGC} &= (\text{LGC} + 0.09 \pm 0.07) / (1.24 \pm 0.07) \\ \text{UVIS: } \text{UGC} &= (\text{LGC} + 0.14 \pm 0.04) / (1.30 \pm 0.04) \\ \text{ALL: } \text{UGC} &= (\text{LGC} + 0.13 \pm 0.04) / (1.30 \pm 0.04) \end{aligned}$$

It is interesting to note that the increased spread in the lensed Gini coefficient relative to the unlensed Gini coefficients suggests that there is more spatial information available in the lensed images, as one might expect because of the additional magnification. However, the fact that they are so similar to the unlensed Gini coefficients also suggests that most of the structure that determines the Gini coefficient is still visible at the resolution used for the unlensed galaxies. This should not be surprising, however, since previous studies have shown that HST-like resolutions are sufficient to extract meaningful morphological information from the Gini coefficient of galaxies even up to $z \approx 4$ (Lotz et al. 2006). This means that it should be possible to use the Gini coefficient to compare samples of strongly lensed galaxies to their unlensed counterparts at similar redshifts, allowing questions of selection effects in strongly lensed samples to be better addressed.

It is also worth noting that both the lensed and unlensed values of the Gini coefficients typically extended to higher values in the bluer filters even though the Gini coefficients behaved similarly near the lower end of the range in all filters. This relationship persisted even when the images originally taken in the F606W filter were convolved with a wider Gaussian to achieve a PSF similar to that of the F160W filter. This suggests that the effect actually has an astrophysical interpretation and is not just the result of PSF convolution and pixelization. If, for example, young and old stellar populations are spatially distributed with different uniformity in a particular galaxy, a mismatch between the Gini coefficients across these two filters would be expected. If this were the case, then it indicates that comparing Gini coefficients measured in different filters may yield further information about the morphology and stellar structure of a galaxy.

3.2. Gini Coefficients and the Effect of S/N Ratio

We have seen in the previous section that the standard deviation of the Gini coefficient in different model real-

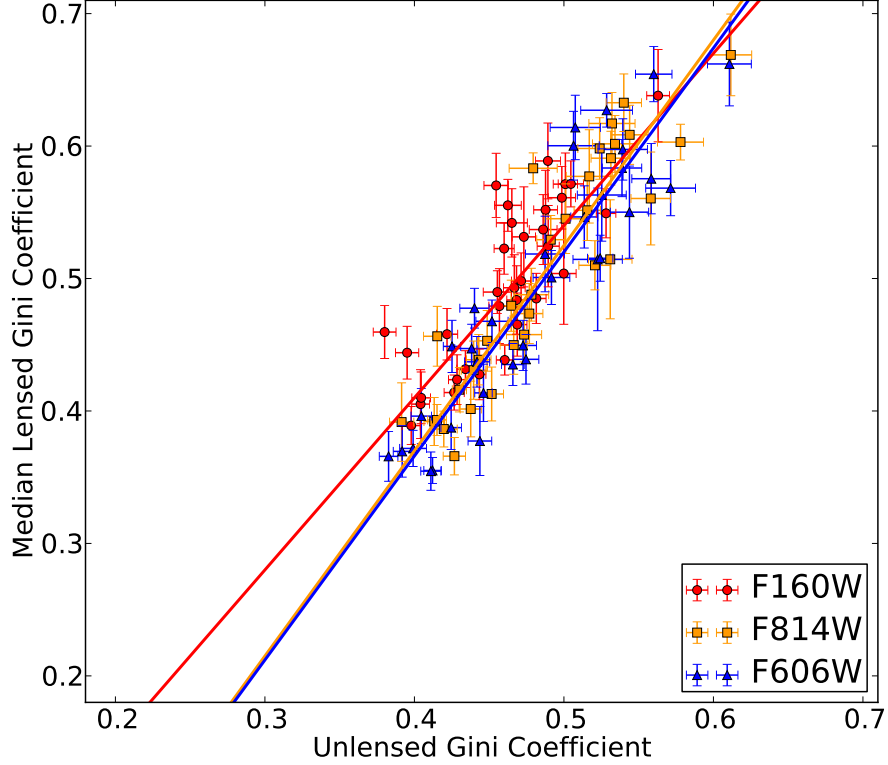


FIG. 3.— Median lensed Gini coefficients plotted against the unlensed Gini coefficients for all filters, using arcs with average S/N per pixel of 0.1. A relationship between unlensed and lensed gini coefficients is evident, though the exact relationship may depend on the filter (likely due to differences in PSF).

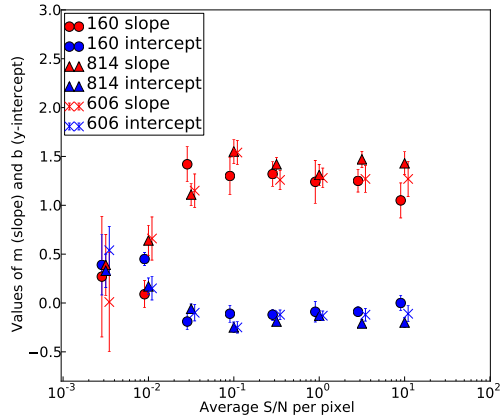


FIG. 4.— Values of the slope and y intercepts of the best fitting lines for lensed vs. unlensed Gini coefficient plots like the one in Fig. 3, but for values of average S/N per pixel between $10^{-2.5}$ and 10. Note that at each S/N level, a small offset has been artificially introduced for each filter, to aid in clarity by preventing points from overlapping with each other. There is little change in these parameters until S/N per pixel drops below $10^{-1.5}$.

izations of the same lensed source galaxy is small relative to the overall dispersion of the median lensed Gini coefficients of the 33 different source galaxies. This means that the Gini coefficient can often be used to distinguish between the lensed images of different source galaxies. However, it is easy to see that in the extreme case where

the average S/N per pixel is very low, the noise will dominate the Gini coefficient measurement and the Gini coefficients of the 33 different galaxies will begin to converge. The natural question to ask is: what is the minimum average S/N per pixel level required for the conclusions of section 3.1 to hold? To test this, we plot the dispersion of the 33 median Gini coefficients against average S/N per pixel. That is, from all of the measured strongly-lensed images of each galaxy, we calculate the median Gini coefficient, and take the standard deviation of the 33 medians (one for each galaxy). When noise is not the dominant source of flux (i.e., when the galaxies' Gini coefficients are discernibly different), we should expect a high dispersion, but the dispersion should tend toward zero as the S/N level decreases. This is borne out in Fig. 6 (where uncertainties in the dispersion are calculated by bootstrapping). It appears that the Gini coefficient is most informative at average S/N per pixel levels greater than or equal to about 0.1.

3.3. Lensed Gini Coefficients of Multiply-Imaged Sources

One way to check the stability of the Gini coefficient under gravitational lensing using real observational data would be to compare the Gini coefficients of galaxies that have been lensed in such a way as to produce multiple images. This can also be done with the simulated images. We have taken pairs from multiple-image configurations and subtracted their Gini coefficients. The his-

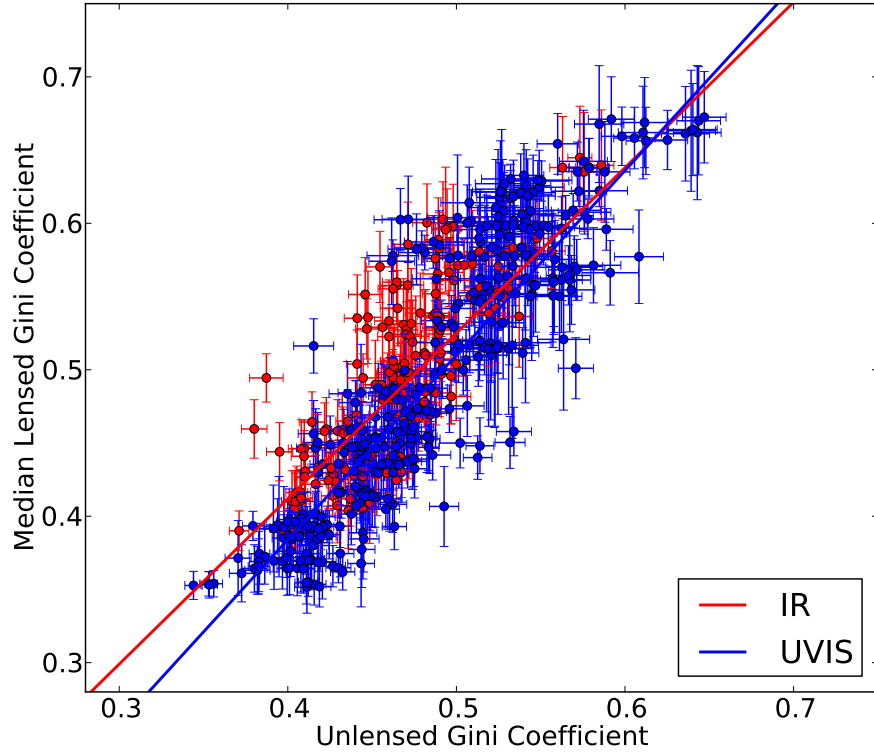


FIG. 5.— Median lensed Gini coefficients plotted against unlensed Gini coefficients for all filters, with UVIS filters in blue and the IR filter in red. Maximum likelihood lines are plotted for the UVIS filters (in blue) and the IR filters (in red). All values of average S/N per pixel of $10^{-1.5}$ and higher are used. The parameters for these best fit lines are given in section 3.1.

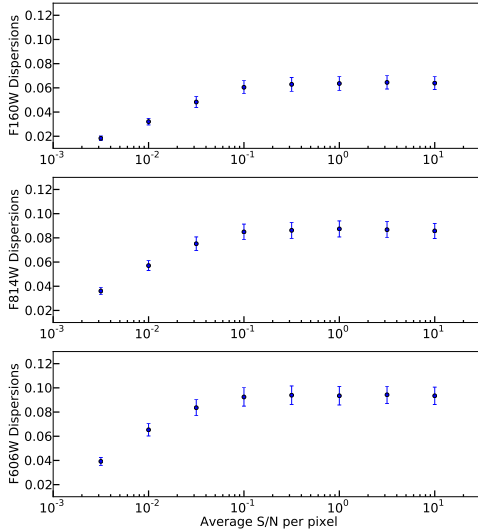


FIG. 6.— The dispersion in the 33 median Gini coefficients at each S/N level. As S/N drops, the Gini coefficients for each galaxy approach the same value, but at high S/N levels, the dispersion in the Gini coefficients of the 33 distinct galaxies is much higher.

togram of the resulting distribution for the S/N = 0.01 per pixel subsample is shown in Fig. 7. Because the Gini coefficients were picked in random order, the distribution contains both negative and positive values and is,

predictably, centered at zero. However, examining the spread of these differences in Gini coefficient, we see that the standard deviation is only about 0.015 while the total range in Gini coefficients as seen in Fig. 3 runs from just under 0.4 to just over 0.6 (though these are medians—some individual images have gini coefficients that range closer to 0.3 or 0.7). This shows that the Gini coefficients of different images of the same galaxy should be expected to be consistent with each other, and that any differences are small compared to the differences possible based on actual structural differences between two different galaxies. Furthermore, it seems that differences in Gini coefficient due to changes in differential magnification from one realization to another are small.

4. CONCLUSIONS

At HST resolutions, the Gini coefficients of galaxies at high redshifts are well-preserved under strong gravitational lensing. However, because of PSF effects and pixelization, the conservation is not perfect. Fortunately, these effects are relatively minor, and can easily be calibrated out. A small deviation from the Gini coefficient in the unlensed frame exists, manifesting as an increased slope and scatter in the plot of lensed vs unlensed Gini coefficients in the studied range of about 0.2 to about 0.7, but scatter off of the trendlines and a slope of greater than 1 is not unreasonable because of the extra spatial information captured in the strongly lensed images. However, the differences in the trendlines for the IR and UVIS subsamples and between those subsamples and the entire

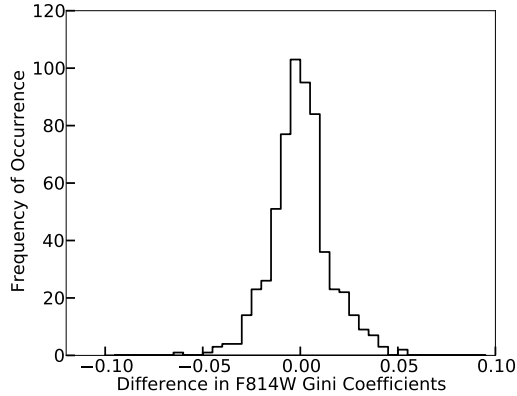


FIG. 7.— The distribution of differences in F814W Gini coefficients between pairs of images from all lensing configurations in the sample for which there are multiple images produced. The order of the pairs is selected randomly, leading to both negative and positive values. The average S/N per pixel for arcs used in this figure was 0.1. The narrowness of this distribution confirms that different images of the same galaxy should have very similar Gini coefficients even when strongly gravitationally lensed.

ensemble are only marginal.

Since a relationship between unlensed and lensed Gini coefficients exists, and because unlensed Gini coefficients continue to carry morphological information out to redshift 4 (Lotz et al. 2006), we can begin to contextualize the existing samples of lensed galaxies like those in the Sloan Giant Arcs Survey (SGAS) sample (e.g., Bayliss et al. 2011, 2014; Sharon et al. 2014) or the Hubble Frontier Fields (Lotz et al. 2014; Koekemoer et al. 2014) with their unlensed counterparts imaged across redshifts in deep field surveys like the Hubble Ultra Deep Field, CANDELS, and others. Additionally, the preservation of

the Gini coefficient in the image plane provides morphological information that can be used as a constraint for identifying image families for the purposes of lens modeling (Florian et al. 2015) in, for example, the Frontier Fields clusters.

Most importantly, we have shown that the Gini coefficient is indeed a meaningful measurement of galaxy morphology that can be conducted in the image plane—no source plane reconstruction is necessary, which means that no lens model is needed. Lens modeling and source plane reconstruction are processes that are time and resource intensive (including both astronomers and telescopes), so measurements like the Gini coefficient, which can be made in the image plane and in only one filter, provide workarounds for one of the most substantial bottlenecks in the process of understanding the morphology of high redshift galaxies. While some applications will still require lens modeling and source plane reconstruction, there is certainly morphological information that can be gleaned from strongly lensed images without these extra steps.

Argonne National Laboratory’s work was supported under the U.S. Department of Energy contract DE-AC02-06CH11357.

This work was supported in part by the Kavli Institute for Cosmological Physics at the University of Chicago through grant NSF PHY-1125897 and an endowment from the Kavli Foundation and its founder Fred Kavli, and by the Strategic Collaborative Initiative administered by the University of Chicago’s Office of the Vice President for Research and for National Laboratories.

REFERENCES

- Abraham, R. G., Tanvir, N. R., Santiago, B.X., et al. 1996, *MNRAS*, 271, 47
- Abraham, R. G., van den Bergh, S., & Nair, P. 2003, *ApJ*, 588, 218
- Bayliss, M. B., Rigby, J. R., Sharon, K., et al. 2014, *ApJ*, 790, 144
- Bayliss, M. B., Gladders, M. D., Masamune, O., et al. 2014, *ApJ*, 790, 144
- Blanton, M. R. et al. 2001, *AJ*, 121, 2358
- Conselice, C. J. 2003, *ApJS*, 147, 1
- Dressler, A. 1980, *ApJ*, 236, 351
- Florian, M., Gladders, M., Li, N., Sharon, K. 2015, (in preparation)
- Galametz, A., Grazian, A., Fontana, A., et al. 2013, *ApJ*, 206, 10
- Jones, T.A., Swinbank, A.M., Ellis, R.S., Richard, J., Stark, D.P. 2010, *MNRAS*, 404, 124
- Jones, T., Ellis, R.S., Richard, J., Jullo, E. 2013, *ApJ*, 765, 48
- Koekemoer, A. M., Avila, R. J., Hammer, D., et al. 2014, *AAS*, 223, 254.02
- Li, N., et al. 2015 (in preparation)
- Lisker, T. 2008, *ApJS*, 179, 319
- Lotz, J.M., Madau, P., Giavalisco, M., Primack, J., Ferguson, H.C. 2006, *ApJ*, 636, 592
- Lotz, J. M., Bountain, M., Grogin, N. A., et al. 2014, *AAS*, 223, 254.01
- Papovich, C., Giavalisco, M., Dickinson, M., Conselice, C. J., Ferguson, H. C. 2003, *ApJ*, 598, 827
- Lefor, A.T., Futamase, T., Akhlaghi, M. 2013, *NewAR*, 57, 1, 1
- Sharon, K., Gladders, M. D., Rigby, J. R., et al. 2014 *ApJ*, 790, 50
- Swinbank, A.M., Webb, T.M., Richard, J., et al. 2009, *MNRAS*, 400, 1121
- Willet, K. W., Schawinski, K., Simmons, B. D., et al. 2016, *MNRAS*, 449, 820
- Wuyts, E., Ribby, J.R., Gladders, M.D., Sharon, K. 2014, *ApJ*, 781, 61
- Yasuda, N. et al. 2001, *AJ*, 122, 1104